Ceramics International 45 (2019) 1084–1092

Contents lists available at ScienceDirect

Ceramics International

journal homepage: www.elsevier.com/locate/ceramint

Atomic layer deposited-ZnO@3D-Ni-foam composite for Na-ion battery anode: A novel route for easy and efficient electrode preparation

Soumyadeep Sinha[a], Pravin N. Didwal[a], Dip K. Nandi[b], Jae Yu Cho[a], Soo-Hyun Kim[b], Chan-Jin Park[a], Jaeyeong Heo[a,*]

[a] *Department of Materials Science and Engineering, and Optoelectronics Convergence Research Center, Chonnam National University, Gwangju 61186, Republic of Korea*
[b] *School of Materials Science and Engineering, Yeungnam University, 214-1, Dae-dong, Gyeongsan-si 38541, Republic of Korea*

ARTICLE INFO

Keywords:
Atomic layer deposition
Na-ion battery
Anode
ZnO@Ni-foam composite
Cycling stability

ABSTRACT

The sluggish kinetics of relatively larger Na-ion still limits the performance of sodium-ion batteries (SIBs) as compared to lithium-ion batteries (LIBs). In this context, a novel route is introduced by coating a thin films of ZnO on a porous 3D Ni-foam scaffold by atomic layer deposition (ALD) for the first time and is used as a superior anode for SIBs without any post-modifications. The scanning electron microscopy along with transmission electron microscopy studies reveal that highly crystalline ZnO can be deposited on such complex 3D Ni-foam with excellent uniformity and conformality. A stable reversible capacity of ~65.1 mAh g^{-1} up to 400 charge-discharge cycles and the excellent rate capability in a wide current density range (30–1000 mA g^{-1}) establish the potential of this composite prepared by a direct and relatively easier method of electrode fabrication. The predominant alloying-dealloying based reactions for Zn-based anode material is also established in SIBs by the post-cycling X-ray photoelectron spectroscopic analyses. The post-cycling analysis of these anodes also reveals the robust structure with good adhesion of the ALD grown films on Ni-foam. In addition, similar study on 2D substrate elucidates the extra advantages of this current strategy. This model efficient route can easily be extended and adopted for any other materials to further enhance the performance of SIBs in future.

1. Introduction

Sodium-ion batteries (SIBs) are receiving increasing attention among researchers, primarily due to the very high abundance of Na compared to Li, which makes them more attractive than their Li-ion counterparts (LIBs); the estimated levels of Li and Na in the Earth's crust are 20 and 236,000 ppm, respectively [1]. While considerable research has already been carried out in this area [2], one of the remaining bottlenecks is the slower kinetics of the larger Na-ion during the sodiation process [2]. To overcome this issue, sodiated transition metal layered oxides (NaT_MO_2: T_M = Ti, V, Cr, Mn, Co, *etc.*, or a combination of 2–3 of these elements) have been explored as cathode materials, while carbonaceous materials and transition metal oxides (sulfides) were found to be suitable anode-material candidates [2,3]. Fe_2O_3, Fe_3O_4, Co_3O_4, SnO_x, Cu_xO, FeS_x, CoS_x, MoS_2, and ZnS, among others, are potential compounds for use as SIB anodes [2]. Nevertheless, drawbacks such as poor reversible capacity, capacity retention, and the structural stabilities of different component materials still require improvement. However, recent studies showed the superior performance of SIBs (power and cycling stability) at low temperature (−30 and 0 °C, respectively) compared to LIBs [4]. Such study truly shows the promising future of SIBs as an alternative to the existing LIBs industry.

On the other hand, the unwanted extra mass loading during conventional electrode fabrication adds additional electrical resistance, in turn decreasing the capacity of the cell whether it is LIBs or SIBs. Optimizing the mass loading of the active electrode material is therefore an important aspect, especially in SIBs. In this regard, atomic layer deposition (ALD) is one of the most efficient techniques for depositing the optimum amount of active electrode material [5–7]. Despite ALD being extensively applied to Li-based batteries, there are very few reports of its use in SIBs [8–17]. Earlier LIB studies showed that capacity was enhanced when active electrode materials were coated on 3D conducting scaffolds, such as multi-walled carbon nanotubes (MWCNTs) by ALD [5–7,18]. However, for MWCNTs, an additional solid current collector, such as a stainless steel (SS) disk, is also required. This issue is addressed by the adoption of 3D Ni-foam (NF) as the current collector. Recently, ALD was very efficiently used to coat an active electrode material on NF substrates to obtain superior electrochemical supercapacitors [19,20]. There are also several reports which demonstrate the superiority of using NF as a self-standing 3D current

---

[*] Corresponding author.
E-mail address: jheo@jnu.ac.kr (J. Heo).

https://doi.org/10.1016/j.ceramint.2018.09.289
Received 20 August 2018; Accepted 28 September 2018

collector for battery electrodes. Unfortunately, all of them used some wet-chemical synthesis routes to coat the NF with the active electrode material [21–26]. Therefore, these previous attempts could be considered inefficient for the conformal and uniform coating compared to ALD. With this in mind, we chose to deposit ZnO in our novel approach, since the ALD reaction mechanism between diethylzinc (DEZ) and H_2O is well-established [27]. In addition, ZnO has not been much explored in SIBs; however, there are reports that showcase ZnO as a promising anode material in LIBs [28–30], and the ALD process has also been used to deposit ZnO films, while in most of these cases different C-based materials, such as graphite, carbon black, graphene *etc.* were used as the substrate for ZnO anode [31–33]. Another reason to choose this ZnO for this study is to explore the possible reaction mechanism of ZnO with Na-ion with post-cycling characterizations of the electrode. The alloying-dealloying based reactions for ZnO anodes in LIBs are well established and a recent report on zinc stannate ($ZnSnO_3$) also proposes similar kind of reaction between Zn and Na in SIBs as well [34]. However, there was no experimental evidence against it that might be difficult due to the presence of similar alloying-dealloying reaction between Sn and Na. Therefore, this attempt gives us a scope to look into the mechanism explicitly for the ZnO/Zn with Na.

In this article, ALD-ZnO@NF was prepared as a model composite material to establish an alternative and efficient route to prepare SIB anode. While ALD-grown ZnO is tested in a Na-ion battery for the first time, the advantages of ALD on a self-standing 3D conducting scaffold, such as NF, is also explored. To realize the benefits of this approach, similar experiments are also carried out on stainless-steel (SS) substrates. Further, the stability of such a 3D composite was confirmed through electrochemical experiments, as well as post-testing analyses. The sodiation and desodiation reaction mechanism between ZnO and Na is also proposed with the experimental evidences.

2. Experimental details

2.1. Synthesis of the atomic layer deposited electrode material

Zinc oxide (ZnO) thin films were deposited by atomic layer deposition (ALD) at 150 °C in a laminar-flow-type thermal ALD reactor (NCD, Lucida D100, Korea) using the well-known ALD-deposition chemistry of diethylzinc (DEZ, EG Chem., Korea) and deionized (DI) water as the ALD precursors of Zn and O, respectively. DEZ was maintained at room temperature, whereas the H_2O was maintained at 10 °C during the deposition process. A continuous 50-sccm flow of N_2 was used as the purging and carrier gas during the deposition process. A ZnO ALD cycle consisted of a DEZ pulse for 0.2 s, N_2 purging for 10 s, a H_2O pulse for 0.2 s, and N_2 purging for 20 s. The two separate surface half-reactions for the ZnO-ALD process can be represented as:

$$ZnOH^* + Zn(CH_2CH_3)_2 \rightarrow ZnOZn(CH_2CH_3)^* + CH_3CH_3 \quad (A)$$

$$Zn(CH_2CH_3)^* + H_2O \rightarrow ZnOH^* + CH_3CH_3 \quad (B)$$

where "*" denotes a surface species.

ZnO thin films were directly deposited on the Ni-foam (NF) substrate by ALD under the same deposition conditions described above. The NF substrates were first sonicated in acetone for 10 min, and then etched in 1 M HCl aqueous solution for 10 min followed by sonication in ethanol for 10 min after washing with DI water [26]. The substrates were finally cleaned with DI water and dried under a flow of N_2 before being placed in the ALD chamber.

2.2. Material characterizations

The crystallinity of the as-deposited film on SS substrate was examined by glancing angle X-ray diffraction (GAXRD) at $\omega = 0.5°$ using high resolution X-Ray diffractometer (PANalytical, X′Pert PRO MPD with Cu kα radiation of 1.542 Å). X-ray photoelectron spectroscopy (XPS, VG Multilab 2000 X-ray photoelectron spectrometer equipped with an Al Kα source) was used to determine the chemical compositions of the constituent elements of the ZnO film on NF substrate, and individual elemental XPS peaks were deconvoluted using the CasaXPS fitting software. The surface morphologies of the as-deposited and post-cycling films on the SS substrates were investigated by scanning-electron microscopy (SEM, Hitachi S-4700). Top-view SEM images of the ZnO thin film deposited on the NF substrate were obtained using focused-ion-beam scanning-electron microscopy (FIB-SEM; FEI, Quanta 3D FEG) during sample preparation for transmission-electron microscopy (TEM). The FIB lift-out technique was used to prepare each sample for cross-sectional TEM analysis. The ZnO@NF composite electrodes were subjected to cross-sectional TEM and energy-dispersive spectroscopy (EDS) (JEOL, JEM-2100F equipped with 200 kV field emission gun) to investigate structures and elemental distributions before and after electrochemical cycling.

2.3. Electrochemical cell fabrication and characterizations

The as-deposited ZnO@NF composites were punched into16-mm-diameter disks that were directly used as working electrodes without any further binder or conductive medium. The mass loading of the active material (ZnO) was determined by weight difference before and after ZnO deposition. CR2032 coin cells were fabricated with the Na/electrolyte/ZnO cell configuration, in which the active ZnO and metallic-Na foil materials were used as the working and counter/reference electrodes, respectively. All cells were assembled inside a glove box that was filled with Ar gas prior to cell fabrication. A porous glass fiber (Whatman) was used as the electrolyte-containing separator. The electrolyte was composed of 1 M $NaClO_4$ in propylene carbonate (PC) with 2% fluoroethylene carbonate (FEC) as an additive. The cells were subjected to cyclic voltammetry (CV, SP-150, Biologic, France) at a scan rate of 0.2 $mV\,s^{-1}$ in the 0.01–3.0 V (*vs.* Na/Na^+) operating-voltage range and the electrochemical impedance spectroscopy (EIS) in the frequency range 100 kHz to 0.01 Hz. Galvanostatic charge–discharge profiles were obtained using a battery-testing unit (WBCS 3000, Won-A-Tech, Korea) in the same potential range used for CV. All electrochemical experiments were performed at room temperature.

3. Results and discussion

3.1. Material characterizations

A schematic representation comparing ALD-ZnO grown on the 3D-NF and 2D-SS substrates and subsequent battery assembly are depicted in Fig. 1; this schematic image clearly highlights the advantages of the direct ZnO-thin-film deposition on 3D-NF substrate, which was then directly used to assemble the battery without any additional binder, conductive agent, or current collector. The multiple layers in the commercial NF with macro-pores easily enable the ALD-grown ZnO to be coated in and through the complete surface available which will be manifolds compared to the only top-surface available in case 2D-SS substrate used as a current collector. Therefore, the similar mass loading in case of a NF substrate requires much less number of ALD cycles with a further increment in the surface to mass ratio.

The XRD patterns of the as-deposited ZnO film on the SS substrate and the bare SS substrate were obtained in glancing-incidence-angle ($\omega = 0.5°$) configurations within the 25–70° 2θ range, the results of which are displayed in Fig. 2a. It clearly reveals that the as-deposited ZnO film is polycrystalline. All the peaks are consistent with the hexagonal wurtzite structure of ZnO (JCPDS No. 036-1451).

The ZnO@NF composite was subjected to the XPS in order to investigate the chemical nature of the constituent elements. The $Ni2p_{3/2}$ and $Ni2p_{1/2}$ XPS peaks at the binding energy of 852.8 and 870 eV along with their satellite peaks at 859 and 874.6 eV, respectively, which correspond to the metallic Ni substrate, are shown in Fig. 2b [35–38].

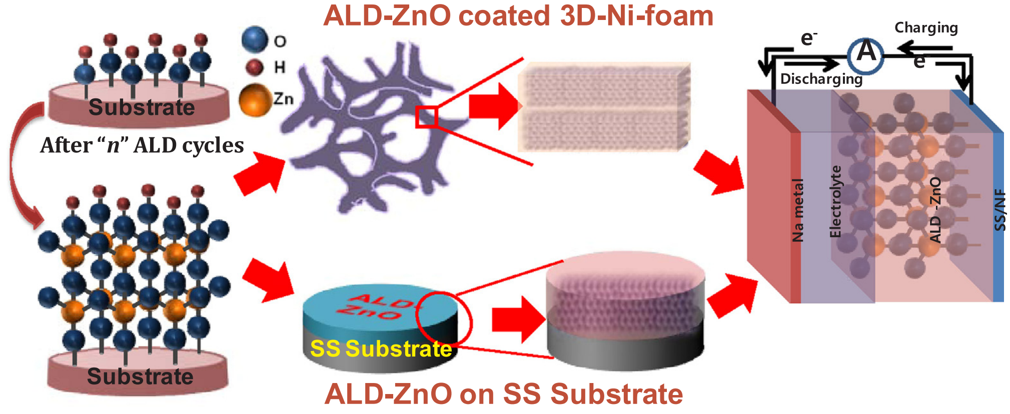

Fig. 1. Illustrating the ALD growth of a material on a 3D-NF and 2D-SS substrates and the subsequent fabrication of an electrode in a half-cell configuration against Na.

The Zn2p$_{3/2}$ peak of ZnO (Fig. 2c) was found to have a binding energy of 1021.5 eV, which is typical of Zn^{2+} in ZnO [32,39]. The O1s XP spectrum (Fig. 2d) displays three deconvoluted peaks centered at 530.1, 531.4, and 532.2 eV. The fitted peak of high intensity at the lower binding energy of 530.1 eV is attributed to lattice O^{2-} involved in Zn–O bonding in the wurtzite ZnO structure [30,32,39]. The shoulder O1s peak at 532.2 eV usually indicates chemisorbed or hydroxyl oxygens on the ZnO surface [30,39]. In addition, another peak at 531.4 eV is observed, which arises due to O^{2-} deficiencies in the ZnO matrix that generally act as sources of conductivity in ZnO films [39,40]. On the basis of the XPS analyses, we conclude that ZnO was successfully grown on the NF.

Fig. 3a displays top-view scanning electron microscopy (SEM) images of the ALD-grown ZnO film on the 3D-NF substrate, which

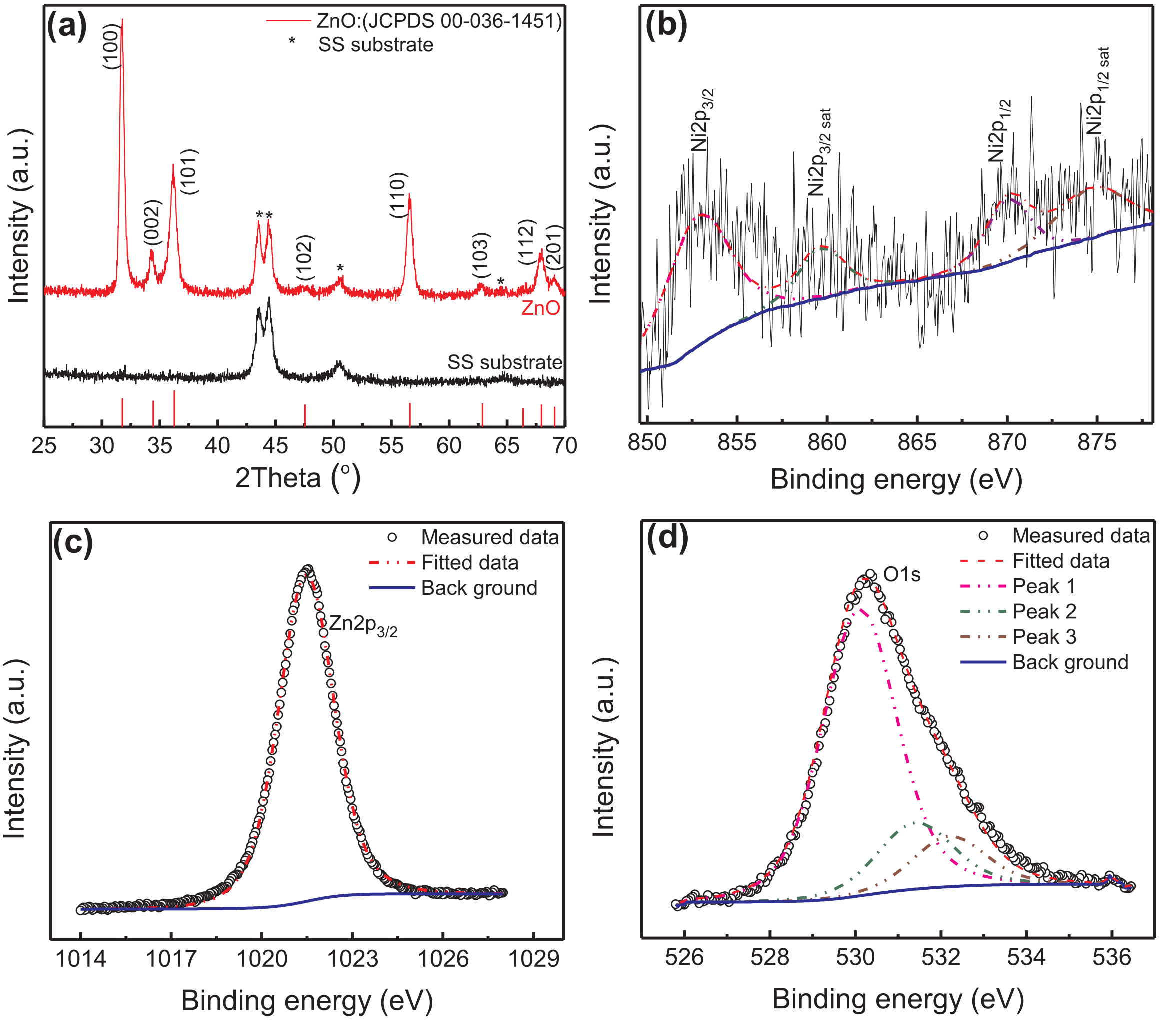

Fig. 2. (a) XRD pattern of the bare and ZnO-coated SS substrate showing the highly poly-crystalline growth of ALD-ZnO on this substrate, (b) Ni2p, (c) Zn2p$_{3/2}$, and (d) O1s XPS spectra of the ALD-grown ZnO thin film on NF.

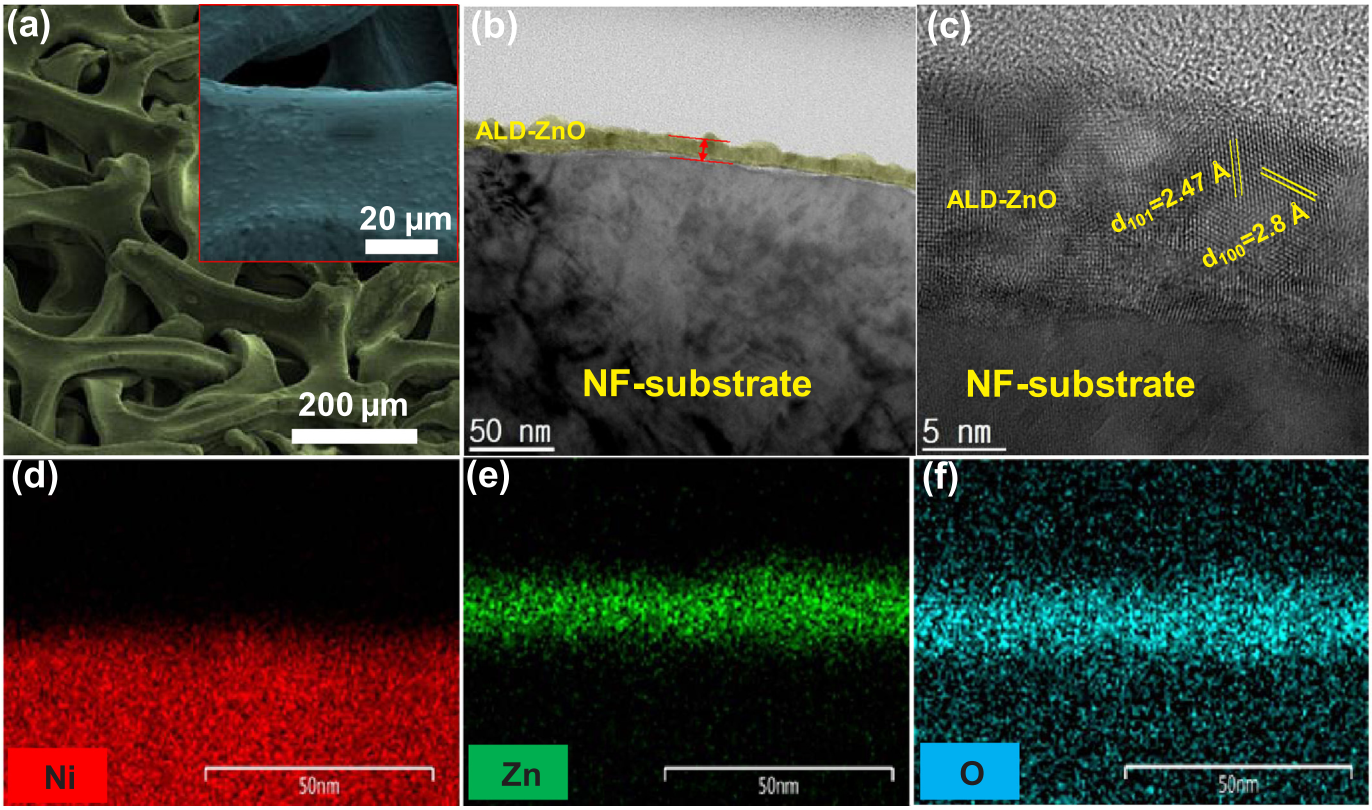

Fig. 3. (a) Top-view SEM images, (b) cross-sectional TEM image, and (c) HRTEM micrograph of uniform and crystalline ALD-ZnO on NF, (d-f) TEM-EDS elemental maps of the composite.

reveal that a highly uniform and conformal film was deposited by ALD on the 3D-NF substrate. However, no specific morphology was observed in these SEM images.

The cross-sectional transmission electron microscopy (TEM) image of this composite is shown in Fig. 3b. An extremely uniform and conformal ZnO thin film, with a thickness of ~ 15 nm, is clearly observed on the 3D-NF substrate, which highlights the capabilities of the ALD process, even for a 3D-substrate. The high-resolution TEM (HRTEM) micrograph of the composite clearly reveals its polycrystalline nature, as shown in Fig. 3c. The lattice fringes provide interplanar distances of ~ 2.47 and 2.8 Å, which correspond to the (101) and (100) planes of the hexagonal wurtzite structure of ZnO (JCPDS Ref. 00-036) and is in good agreement with our XRD analysis of the ZnO@SS film (Fig. 2a). Therefore, it could also be concluded here that the growth and the crystalline properties of the ALD grown ZnO does not depend on the different substrates used in this study. Further, the cross-sectional TEM-EDS elemental maps of the ZnO@NF composite are displayed in Fig. 3d–f. The uniform distribution of Zn and O on the Ni (Fig. 3d) substrate is clearly evident in Fig. 3e and f. Hence, the cross-sectional TEM image, along with the EDS analysis, confirms growth of polycrystalline ZnO on the 3D-NF substrate and highlights the superiority of the ALD process compared with other thin-film-deposition techniques.

3.2. *Electrochemical performances of ALD-ZnO as anode*

Fig. 4 displays the electrochemical performance of the ZnO@NF electrodes. The ZnO@NF electrode was subjected to cyclic voltammetry (CV) in order to understand its electrochemical behavior during the sodiation/desodiation process against Na metal. Fig. 4a displays the CV trace over the first five consecutive cycles at a scan rate of 0.2 mV s^{-1} in the 0.01–3.0 V (*vs.* Na/Na$^+$) potential range. The first cathodic CV sweep encompasses the reduction process in which the conversion of ZnO into elemental Zn takes place followed by alloying with sodium to form NaZn$_x$, which is encapsulated in the Na$_2$O matrix. Similar phenomena have been observed for other metal-oxide-based anode materials in SIBs [34,41,42]. The matrix acts as a buffer during the alloying-dealloying reactions; hence, the electrochemical reactions in the ZnO half-cell are proposed to be:

$$ZnO + 2Na^+ + 2e^- \rightarrow Zn + Na_2O \quad (1)$$

$$Zn_x + Na \rightarrow NaZn_x \quad (2)$$

The broad strong reduction peak below 1 V is therefore ascribed to the formation of a solid electrolyte interface (SEI) layer and the Na-Zn alloy (NaZn$_{13}$), while a small hump at ~ 1.3 V might correspond to the ZnO→Zn conversion reaction and the formation of the Na$_2$O phase [43]. The significant amount of irreversible conversion of ZnO into Zn metal (Eq. (1)), followed by the reversible alloying reaction with Na during further reduction (Eq. (2)), or the sodiation of the ZnO@NF electrode, results in a high capacity loss after the first cycle. However, a certain amount of this metallic Zn is also expected to undergo the reversible ZnO formation by the oxidation reaction during anodic sweep (charge cycle). From second cycle onwards, two distinct reduction peaks are evident in the CV which could be assigned to the two simultaneous process of the sodiation in the electrode that consist of the conversion of ZnO (which formed reversibly in the first charge cycle) and the alloying formation of Na-Zn at relatively lower potential. Interestingly, the conversion reaction from second cycle onwards is also observed to shift to a lower potential that might be caused by the drastic change in the chemical environment of electrode after the first charge-discharge cycle. However, from the second cycle onwards, ZnO@NF exhibited overlapping cyclic behavior during CV, which is indicative of the stability in the sodiation-desodiation process with similar redox reactions took place in the second cycle.

The galvanostatic charge-discharge cycling performance of the ZnO@NF electrode was further investigated at a current density of

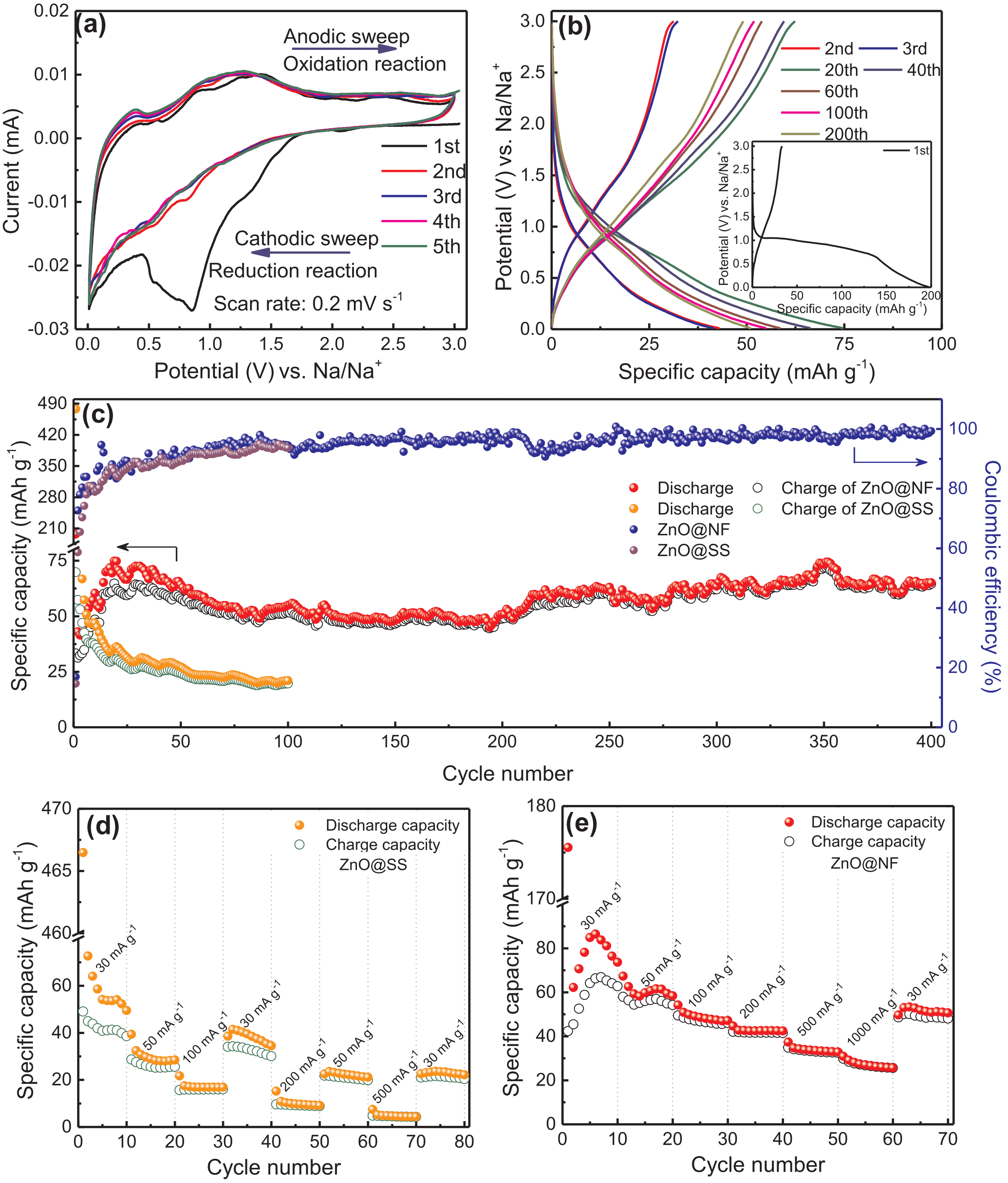

Fig. 4. (a) Cyclic voltammograms of the ALD-ZnO@NF electrode for the first five cycles in the 0.01–3.0 V potential window at a scan rate of 0.2 mV s^{-1}, (b) representative charge-discharge profiles at a current density of 30 mA g^{-1} (Inset shows the first charge-discharge profile), (c) cycling performance comparison between the ZnO@NF and ZnO@SS electrode along with the coulombic efficiencies at a current density of 30 mA g^{-1}, rate capability of the (d) ZnO@SS and (e) ZnO@NF electrodes with large variations in current densities (30–1000 mA g^{-1}).

30 mA g^{-1} in the similar 0.01–3.0 V (*vs.* Na/Na^{+}) potential range. The charge-discharge profile of the ZnO@NF electrode (Fig. 4b) exhibits an initial discharge/charge capacity of 197.3/33.3 mAh g^{-1}, with a high irreversibility of about 83%. The initial capacity loss of the ZnO@NF electrode is attributed to SEI-layer formation, decomposition of the electrolyte, and the irreversible conversion of ZnO into Zn. Although the discharge capacity dropped to 43 mAh g^{-1} during the second cycle, the increase in coulombic efficiency (to 73%) together with a charge capacity of 31.3 mAh g^{-1} indicate that the electrochemical reactions were efficient and reversible during the charge-discharge process after the first cycle. Similar characteristic charge-discharge profiles were observed for the remaining cycles during extended cycling performance testing.

The cycling stability of the ZnO@NF electrode at a current density of 30 mA g^{-1} is shown in Fig. 4c. The ZnO@NF electrode exhibited a discharge capacity of ~ 65.1 mAh g^{-1} with 99.3% coulombic efficiency after 400 cycles; it was essentially stable without any significant capacity fading. Fig. 4c also reveals that the discharge capacity of the ZnO@NF electrode decreased during the second cycle, but slowly increased during consecutive cycles to attain an essentially stable capacity of 74.8 mAh g^{-1} after 20 cycles with an 83% coulombic efficiency; the increase in the capacity over these consecutive cycles is attributed to the activation process [6] and an increase in the interfacial area by surface roughening of the ZnO upon cycling. For electrochemical performance comparison, the similar mass loading (~ 0.3 mg) of ZnO active material was also obtained on SS disk current collector (named as ZnO@SS) with 16-mm diameter by using 1300 ALD cycles which resulted in a uniform thickness of ~ 240–245 nm of ZnO film. The mass loading of the active material (ZnO) on SS substrates were calculated by using the thickness of the ZnO thin films as measured on the Si substrates, which were deposited together during the same reaction process. The calculated density of ZnO thin film was used for this mass calculation as obtained from the XRR measurement. The mass loading value also cross checked by taking the weight of the SS substrates before and after ZnO deposition. In comparison to the ZnO@NF electrodes, the ZnO@SS electrodes with similar mass loading of electrode material delivered a very low specific discharge capacity of ~ 21 mAh g^{-1} after only 100 charge-discharge cycles as shown in Fig. 4c. The poor performance of ZnO@SS electrodes can be primarily attributed to the extremely low surface to volume ratio of it. The ALD on a 2D substrate like SS perfectly leads to end up with a similar 2D dense ZnO without any porosity inside the film. On the other hand, to achieve the similar mass loading (~ 0.3 mg), the deposited film becomes considerably thick that provides highly resistive path for the efficient sodiation in the anode material. The increase in internal resistance in the thick film may result in a mechanical instability of the electrode material which induces the formation of cracks or fracture in the active material due the significant volume change through the sodiation and de-sodiation process during the charge-discharge cycles. It should also be noted that an almost three-fold increase in reversible capacity was observed for the ZnO@NF electrode fabricated using significantly fewer ALD cycles compared to that based on the 2D-ZnO@SS electrode. Therefore, it seems that suitable electronic conduction and the highly porous NF substrate provide a greater number of 3D charge-transport pathways during cycling in the ZnO@NF composite.

Furthermore, we investigated the rate capability of the ZnO@SS and ZnO@NF electrodes at different current densities in the 30–1000 mA g^{-1} range, the results of which are shown in Fig. 4d and e, respectively. Fig. 4e shows an initial discharge capacity of 175.5 mAh g^{-1} during the first discharge at a current density of 30 mA g^{-1} and ~ 73.6 mAh g^{-1} at the 10th cycle for the ZnO@NF electrode. The specific capacities decreased slightly with further increases in current density. The first-cycle discharge capacities of the ZnO@NF electrode were about 67.3, 54.2, 44.7, 37.4, and 30.9 mAh g^{-1} at current densities of 50, 100, 200, 500, and 1000 mA g^{-1}, respectively. Even after cycling at the high current density of 1000 mA g^{-1}, the ZnO@NF electrode retained a favorable average specific capacity value of ~ 51.6 mAh g^{-1} at a current density of 30 mA g^{-1} after 60 cycles, which is around 70% of the capacity observed at the 10th cycle with the same initial current density of 30 mA g^{-1}. While, the ZnO@SS electrode exhibited much lower capacities and poor rate capability as shown in Fig. 4d. Hence, this study reveals that the ZnO@NF electrode delivers rate stability and a remarkably stable cycling life, highlighting the superiority of the ZnO@NF composite as a SIB anode. In addition, we also investigated the rate capability of ZnO@NF electrode with higher mass loading (~ 1 mg) of the active material by using 400 ALD cycles which showed a significant decrease in specific capacity in comparison to the ZnO@NF electrode grown by 100 ALD cycles for all current densities (not shown here). Therefore, a very thin film of any ALD grown active material on 3D-NF is expected to provide an optimum performance in SIBs compared to a much thicker film needed in case of conventional electrode casting on 2D conducting substrates like SS or Cu foils.

To investigate further the kinetics and the improved electrochemical performance of ZnO@NF electrode, the EIS measurements were performed in the frequency range of 100 kHz to 0.01 Hz for both the as prepared electrodes. A comparison between the Nyquist plots of the ZnO@SS and ZnO@NF electrodes is shown in Fig. 5 as obtained from the EIS measurements. A Nyquist plot of an electrochemical system can be assigned in different parts. The semicircle from high to medium frequency corresponds to charge transfer resistance (R_{ct}) between electrode and electrolyte and a typical Warburg behavior can be obtained from the slope of the linear portion at the low frequency region of the curve [26,44–46]. It can be clearly seen from Fig. 5 that the diameter of the semicircle as obtained for the ZnO@NF electrode is smaller than the ZnO@SS electrode whereas the ZnO@SS electrode basically displays an incomplete semicircle which denoting a lower resistance along the interface for ZnO@NF electrode in comparison to the ZnO@SS. Therefore, the network-like ZnO@NF porous structure can be attributed to the higher contact area between the electro active materials and electrolyte which is also favorable for rapid Na^{+} diffusion than the ZnO@SS electrodes.

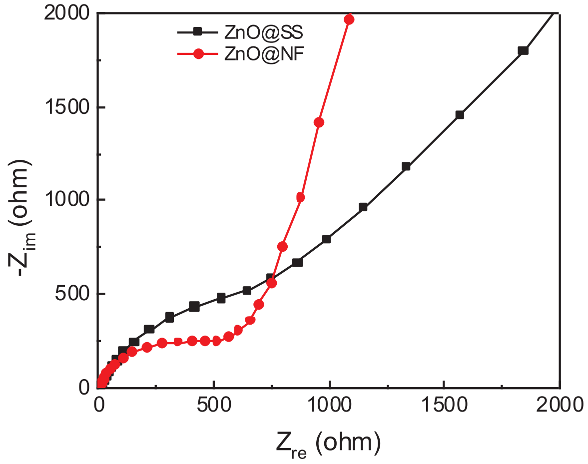

Fig. 5. Nyquist plots obtained from the EIS measurements of as prepared ZnO@NF and ZnO@SS electrodes.

The post-cycling (after 100 discharge-charge cycles) *ex situ* XPS analyses were carried out to understand the possible reactions in the ZnO anode in SIBs. After 100 cycles, the electrodes were dismantled and washed with propylene carbonate to remove the electrolyte salts, after which it were dried overnight under vacuum before analysis. The individual high-resolution XP spectra of Na1s, O1s C1s and Zn2p are shown in Fig. 6. The distinct and prominent presence of Na1s peak primarily confirms the irreversible reaction between the Zn and Na_2O after the conversion reaction takes place during the very first discharge cycle of this anode. As the cell was dismantled for XPS analysis after the complete charge cycle, Na is expected to be absent in the film. In a more practical situation, a small amount of Na would be present. However, Na1s appeared to be one of the strongest peaks in the complete survey of the electrode after cycling (Fig. 6a). The further deconvolution of the Na1s (Fig. 6b) at 1070.8 and 1071.6 eV could be assigned to Na_2CO_3 and Na_2O, respectively [38,47,48], in almost equal percentage. The Na_2CO_3 could either be formed due to the reaction between Na_2O and the propylene carbonate (PC) during the cleaning of the electrode after cycling or could also come from the reaction of electrolyte and PC. The absence of ZnO as a major phase inside the electrode after cycling is confirmed by the significant shift in the O1s peak (Fig. 6c). The relatively broad peak centered at ~ 532.4 eV could be fitted corresponding to O in C-O (in Na_2CO_3), O-H (in NaOH), Zn-O (in ZnO) and Na-O (in Na_2O) at 531.7, 532.9, 530.1, and 529.6 eV, respectively [32,38,48–50]. In addition, the Na KLL Auger peak is also identified along with this O1s at a higher binding energy of it (~ 536.4 eV) that can be ascribed to the Na in Na_2O [48,51]. It is clear from this O1s and associated Na Auger peak that the major contribution is from Na_2O and Na_2CO_3. However, very little amount of ZnO could be there in the electrode resulted from the certain amount of reversible conversion reaction during charge cycle. Therefore, unlike to the complete

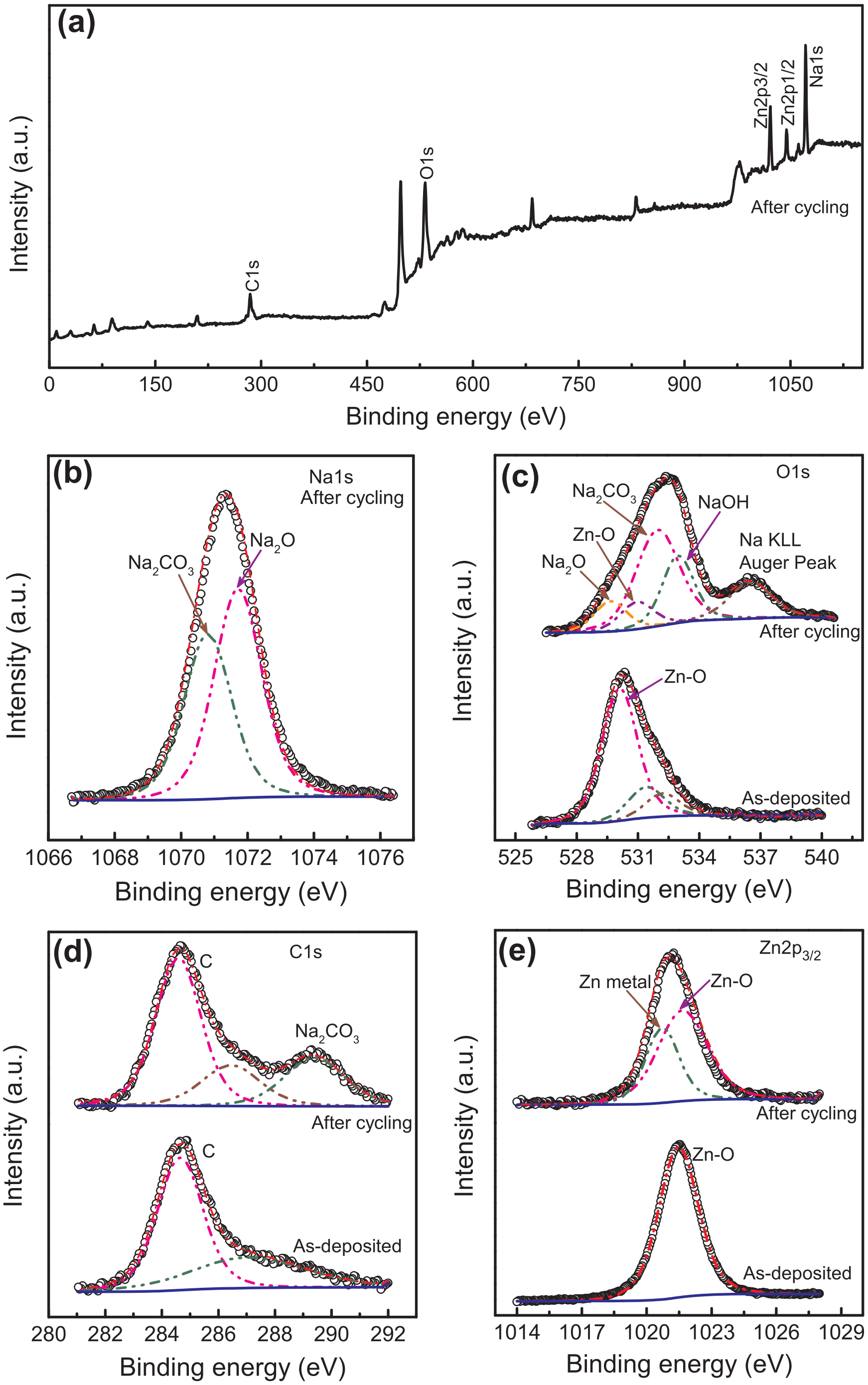

Fig. 6. (a) Full XPS survey, and individual XPS spectra of (b) Na1s, (c) O1s, (d) C1s, and (e) $Zn2p_{3/2}$ after 100 charge-discharge cycle in comparison with as-deposited ZnO@NF electrode.

alloying-dealloying based reaction proposed earlier in the case $ZnSnO_3$ [34], a certain amount of reformation of ZnO would be possible for this case. This proposed activity is further supported by post-cycling TEM analysis as discussed later of this article. Few earlier reported CVs of ZnO anodes in LIBs also showed that the reversible oxide formation after each discharge cycle drastically decreases upon cycling and slowly disappears. However, our study reveals that reversible ZnO formation takes place and a certain amount of capacity, though less, could be contributed by conversion reaction in addition to the reversible alloying-dealloying reaction. Here, we assume that no amount of as-grown ZnO is left unreacted after 100 charge-discharge cycles. As the ZnO film on NF was extremely thin (only ~ 15 nm) in this particular case, such an assumption is well-justified. Similar to the O1s, along with the major peak of C1s, the additional peak centered at 289.4 eV could be assigned to Na_2CO_3 [38,52] as shown in Fig. 6d. All of these further indicate the presence of significant Na_2O which acted as a host matrix for the alloying-dealloying reaction to take place. Moreover, there is a visible shift ($>$ 0.3 eV) that can be observed from Fig. 6e, for the peak corresponding to $Zn2p_{3/2}$ orbital electron towards the lower binding energy. The shift in this $Zn2p_{3/2}$ XP spectrum could only occurr due to the presence of metallic Zn in the electrode after the charge cycle. However, this peak ($Zn2p_{3/2}$) also can be deconvoluted into two peaks corresponding to Zn(0) as metal and to Zn^{+2} in ZnO at 1020.7 and 1021.5 eV, respectively [32,53]. Thus the post-cycling XPS analysis

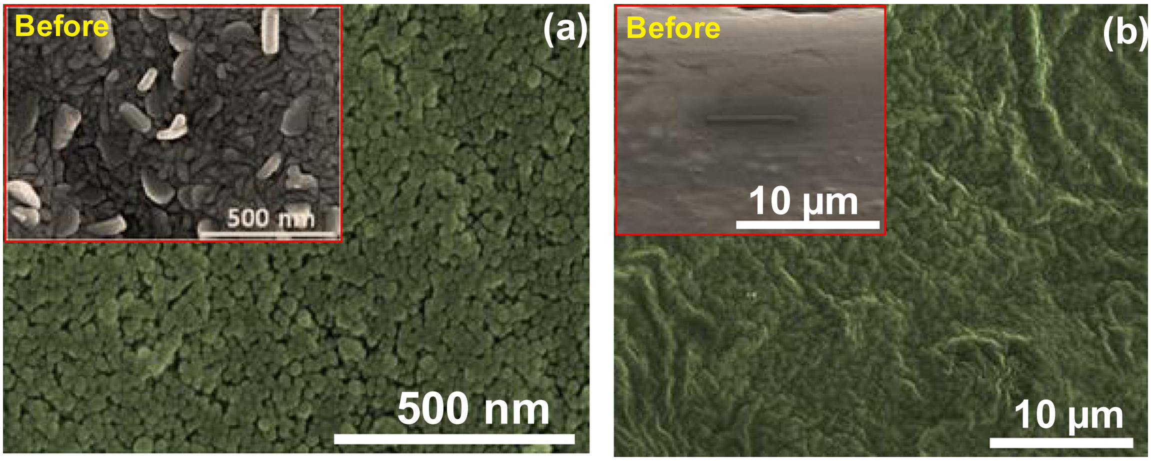

Fig. 7. Top-view SEM images of the (a) ZnO@SS and (b) ZnO@NF after 100 charge-discharge cycles; the insets show the corresponding SEM image prior to battery cycling for comparison.

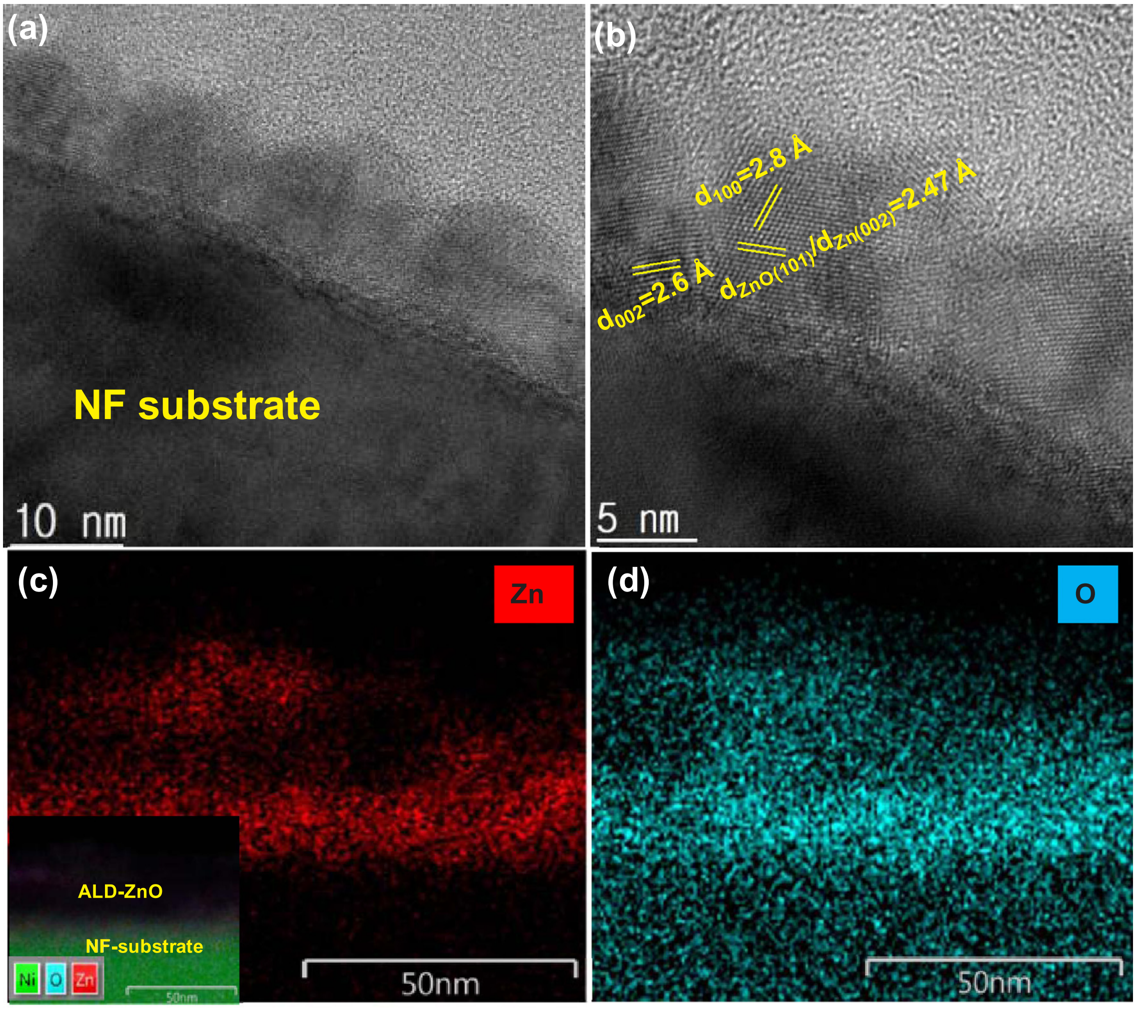

Fig. 8. (a-b) Cross-sectional TEM analysis of the ZnO@NF electrode at the end of 100th charge-discharge cycles revealing relatively less uniform and wavy like ZnO film present on the NF substrate, the TEM-EDS elemental mapping of the composite showing the uniform but relatively scattered presence of both (c) Zn and (d) O.

clearly established the predominant alloying-dealloying reaction between Zn and Na after the first discharge cycle. In addition, a certain amount of reversible ZnO formation during the charge cycle is also highly possible for this particular case.

In addition to the electrochemical studies discussed above, the ZnO@SS and ZnO@NF electrode were examined by SEM after 100 charge-discharge cycles at a current density of 30 mA g^{-1}, the *ex-situ* top-view SEM image is displayed in Fig. 7a and b, respectively. The post-cycling top-view SEM image of the ZnO@NF electrode shows a slightly deformed film surface without any considerable formation of cracks or damage, when compared to the ZnO@SS electrode. The active electrode material was retained almost intact on the 3D-NF substrate, and may be responsible for the superior electrochemical performance observed for the ZnO@NF electrode.

Further post-cycling cross-sectional TEM and EDS analyses were carried out on the ZnO@NF electrode to complement the previous SEM image. Fig. 8a reveals that a uniform layer of the active material is still present on 3D-NF substrate following the cycling experiment. A slight deformation of the film can be observed in the TEM micrographs. The HRTEM image (Fig. 8b) shows the presence of ZnO along with the traces Zn metal, which also supports the post-cycling *ex-situ* XPS analyses as discussed above. However, the material maintained its structural stability and strong adhesion to the NF substrate after the cycling process when compared with the as-deposited material (Fig. 3c).

The performance of the present ZnO@NF electrode is comparable with that very recently reported by Teng et al. on hydrothermal-ZnO [54], which exhibited a specific capacity of 100 and 70 mAh g^{-1} at different current densities. The nominally higher capacity reported by Teng might be attributed to the conductive carbon coating on the ZnO used in their work. On the other hand, zinc stannate ($ZnSnO_3$) shows much higher performance as an anode in SIBs where the majority of the capacity was contributed by the reversible alloying-dealloying reaction between Zn and Sn. Interestingly, the capacity achieved from the only ZnO for this case was as low as ~ 20–25 mAh g^{-1} at 30 mA g^{-1} current density [34]. ALD-grown active electrodes for SIBs are concerned, a crystalline ternary-layered oxide (sodium titanate, $Na_{0.23}TiO_2$) deposited on CNTs exhibited a stable reversible capacity of 28 mAh g^{-1} which is much lower compared to current work without any carbon [55]. Similarly, an optimum 100 cycles ALD-TiO_2 on CNT-CFP (carbon-fiber paper) also delivered about 128.6 mAh g^{-1} at a current density of 2 mA g^{-1} [6]. Therefore, the present results are on par with the existing literature, while introducing a novel approach to combine ALD and NF for the first time in the field of SIBs. Interestingly, a very recent study on ALD-MoS_2 on a SS substrate revealed very high capacities in SIBs [56]. The present approach could be therefore extended to these more-suitable conversion-based transition metal binary compounds to achieve even higher SIB capacities.

4. Conclusion

In this work, ALD-grown ZnO@NF was used to showcase the easy, direct, and efficient preparation of a SIB anode. The extremely uniform and conformal ALD thin-film coating on the NF withstood a current rate of 1000 mA g^{-1} with significant capacity recovery. The ZnO@NF composite yielded a stable ~ 65.1 mAh g^{-1} capacity over 400 cycles. When compared with the similar ALD-grown ZnO on 2D-SS current collector, a three-times-greater reversible capacity was observed after significantly fewer ALD-deposition cycles, highlighting the novelty of this approach. Both reversible conversion and alloying-dealloying reaction mechanism between ZnO and Na was evident from the CVs and supported by the post-cycling analyses of the electrodes. We expect that this model approach of combining ALD and Ni-foam can be further extended to grow any other electrode material in order to enhance SIB performance.

Acknowledgement

This research was supported by the National Research Foundation of Korea (NRF) grant funded by the Korea government (MSIT) (NRF-2018R1A2B6002268, NRF-2018M3A7B4065885) and also supported by the Human Resources Development (20164030201310) of the Korea Institute of Energy Technology Evaluation and Planning (KETEP) granted financial resource from the Ministry of Trade, Industry & Energy, Republic of Korea.

References

[1] N. Yabuuchi, K. Kubota, M. Dahbi, S. Komaba, Chem. Rev. 114 (2014) 11636–11682.
[2] J.-Y. Hwang, S.-T. Myung, Y.-K. Sun, Chem. Soc. Rev. 46 (2017) 3529–3614.
[3] M.H. Han, E. Gonzalo, G. Singh, T. Rojo, Energy Environ. Sci. 8 (2015) 81–102.
[4] K. Mukai, T. Inoue, Y. Kato, S. Shirai, ACS Omega 2 (2017) 864–872.
[5] A. Dhara, S.K. Sarkar, S. Mitra, Adv. Mater. Interfaces 4 (2017) (1700332-n/a).
[6] H. Wang, G. Jia, Y. Guo, Y. Zhang, H. Geng, J. Xu, W. Mai, Q. Yan, H.J. Fan, Adv. Mater. Interfaces 3 (2016) (1600375-n/a).
[7] J. Liu, B. Wang, Q. Sun, R. Li, T.-K. Sham, X. Sun, Adv. Mater. Interfaces 3 (2016) (1600468-n/a).
[8] X. Han, Y. Liu, Z. Jia, Y.-C. Chen, J. Wan, N. Weadock, K.J. Gaskell, T. Li, L. Hu, Nano Lett. 14 (2014) 139–147.
[9] H. Kou, X. Li, H. Shan, L. Fan, B. Yan, D. Li, J. Mater. Chem. A 5 (2017) 17881–17888.
[10] L. Zhao, J. Zhao, Y.-S. Hu, H. Li, Z. Zhou, M. Armand, L. Chen, Adv. Energy Mater. 2 (2012) 962–965.
[11] J. Alvarado, C. Ma, S. Wang, K. Nguyen, M. Kodur, Y.S. Meng, ACS Appl. Mater. Interfaces 9 (2017) 26518–26530.
[12] L. Dong, L. RuiXian, J. Feng, C. Long, G. Wang, H. Kou, M. Zhao, L. Dong, X. Li, D. Li, Mater. Lett. 205 (2017) 75–78.
[13] C. Guan, J. Wang, Adv. Sci. 3 (2016) (1500405-n/a).
[14] X. Sun, C. Zhou, M. Xie, T. Hu, H. Sun, G. Xin, G. Wang, S.M. George, J. Lian, Chem. Commun. 50 (2014) 10703–10706.
[15] J. Zhao, G. Qu, J.C. Flake, Y. Wang, Chem. Commun. 48 (2012) 8108–8110.
[16] X. Meng, X.Q. Yang, X. Sun, Adv. Mater. 24 (2012) 3589–3615.
[17] X. Meng, J. Mater. Chem. A 5 (2017) 10127–10149.
[18] D.K. Nandi, U.K. Sen, S. Sinha, A. Dhara, S. Mitra, S.K. Sarkar, Phys. Chem. Chem. Phys. 17 (2015) 17445–17453.
[19] D.K. Nandi, S. Sahoo, S. Sinha, S. Yeo, H. Kim, R.N. Bulakhe, J. Heo, J.-J. Shim, S.-H. Kim, ACS Appl. Mater. Interfaces 9 (2017) 40252–40264.
[20] H. Li, Y. Gao, Y. Shao, Y. Su, X. Wang, Nano Lett. 15 (2015) 6689–6695.
[21] J. Tang, S. Ni, Q. Chen, W. Han, X. Yang, L. Zhang, Mater. Lett. 195 (2017) 127–130.
[22] L. Wang, C. Wang, F. Li, F. Cheng, J. Chen, Chem. Commun. 54 (2018) 38–41.
[23] X. Song, X. Li, Z. Bai, B. Yan, D. Li, X. Sun, Nano Energy 26 (2016) 533–540.
[24] J.-W. Lee, H.-S. Shin, C.-W. Lee, K.-N. Jung, Nanoscale Res. Lett. 11 (2016) 45.
[25] L. Liu, H. Zhang, Y. Mu, J. Yang, Y. Wang, ACS Appl. Mater. Interfaces 8 (2016) 1351–1359.
[26] X. Wu, S. Li, B. Wang, J. Liu, M. Yu, RSC Adv. 5 (2015) 81341–81347.
[27] T. Tommi, K. Maarit, Semicond. Sci. Technol. 29 (2014) 043001.
[28] H.-Q. Dai, H. Xu, Y.-N. Zhou, F. Lu, Z.-W. Fu, J. Phys. Chem. C 116 (2012) 1519–1525.
[29] J. Xie, N. Imanishi, A. Hirano, Y. Takeda, O. Yamamoto, X.B. Zhao, G.S. Cao, Thin Solid Films 519 (2011) 3373–3377.
[30] Z.-W. Fu, F. Huang, Y. Zhang, Y. Chu, Q.-Z. Qin, J. Electrochem. Soc. 150 (2003) A714–A720.
[31] M. Yu, A. Wang, Y. Wang, C. Li, G. Shi, Nanoscale 6 (2014) 11419–11424.
[32] S. Lu, H. Wang, J. Zhou, X. Wu, W. Qin, Nanoscale 9 (2017) 1184–1192.
[33] Y. Li, Y. Zhao, G. Huang, B. Xu, B. Wang, R. Pan, C. Men, Y. Mei, ACS Appl. Mater. Interfaces 9 (2017) 38522–38529.
[34] L.P. Wang, Y. Zhao, C. Wei, C. Wong, M. Srinivasan, Z.J. Xu, J. Mater. Chem. A 3 (2015) 14033–14038.
[35] G.H. Yu, L.R. Zeng, F.W. Zhu, C.L. Chai, W.Y. Lai, J. Appl. Phys. 90 (2001) 4039–4043.
[36] M. Grden, M. Alsabet, G. Jerkiewicz, ACS Appl. Mater. Interfaces 4 (2012) 3012–3021.
[37] H. Li-Shing, R.S. Williams, J. Phys. Chem. Solids 55 (1994) 305–312.
[38] J.F. Moulder, W.F. Stickle, P.E. Sobol, K.D. Bomben, Handbook of X-Ray Photoelectron Spectroscopy, PerkinElmer Corp., Eden Prairie, Minnesota, 1992.
[39] G.R. Dillip, A.N. Banerjee, V.C. Anitha, B. Deva Prasad Raju, S.W. Joo, B.K. Min, ACS Appl. Mater. Interfaces 8 (2016) 5025–5039.
[40] J. Wang, Z. Wang, B. Huang, Y. Ma, Y. Liu, X. Qin, X. Zhang, Y. Dai, ACS Appl. Mater. Interfaces 4 (2012) 4024–4030.
[41] D. Su, H.-J. Ahn, G. Wang, Chem. Commun. 49 (2013) 3131–3133.
[42] Y. Wang, D. Su, C. Wang, G. Wang, Electrochem. Commun. 29 (2013) 8–11.
[43] F. Xu, Z. Li, L. Wu, Q. Meng, H.L. Xin, J. Sun, B. Ge, L. Sun, Y. Zhu, Nano Energy 30 (2016) 771–779.
[44] C.Q. Zhang, J.P. Tu, Y.F. Yuan, X.H. Huang, X.T. Chen, F. Mao, J. Electrochem. Soc. 154 (2007) A65–A69.
[45] D. Aurbach, J. Power Sources 89 (2000) 206–218.
[46] B. Wang, S. Li, J. Liu, M. Yu, B. Li, X. Wu, Electrochim. Acta 146 (2014) 679–687.
[47] D.A. Cristaldi, C.G. Fortuna, A. Gulino, Anal. Methods 5 (2013) 3458–3462.
[48] H.W. Nesbitt, G.M. Bancroft, G.S. Henderson, R. Ho, K.N. Dalby, Y. Huang, Z. Yan, J. Non-Cryst. Solids 357 (2011) 170–180.
[49] C.D. Wagner, D.A. Zatko, R.H. Raymond, Anal. Chem. 52 (1980) 1445–1451.
[50] A. Barrie, F.J. Street, J. Electron. Spectrosc. Relat. Phenom. 7 (1975) 1–31.
[51] H.W. Nesbitt, G.S. Henderson, G.M. Bancroft, R. Ho, J. Non-Cryst. Solids 409 (2015) 139–148.
[52] R. Würz, M. Rusu, T. Schedel-Niedrig, M.C. Lux-Steiner, H. Bluhm, M. Hävecker, E. Kleimenov, A. Knop-Gericke, R. Schlögl, Surf. Sci. 580 (2005) 80–94.
[53] E. Diler, B. Lescop, S. Rioual, G. Nguyen Vien, D. Thierry, B. Rouvellou, Corros. Sci. 79 (2014) 83–88.
[54] Y. Teng, M. Mo, Y. Li, J. Xue, H. Zhao, J. Alloy. Compd. 744 (2018) 712–720.
[55] J. Liu, M.N. Banis, B. Xiao, Q. Sun, A. Lushington, R. Li, J. Guo, T.-K. Sham, X. Sun, J. Mater. Chem. A 3 (2015) 24281–24288.
[56] M.B. Sreedhara, S. Gope, B. Vishal, R. Datta, A.J. Bhattacharyya, C.N.R. Rao, J. Mater. Chem. A 6 (2018) 2302–2310.